Atmos. Meas. Tech. Discuss., 6, 7911–7943, 2013
www.atmos-meas-tech-discuss.net/6/7911/2013/
doi:10.5194/amtd-6-7911-2013
© Author(s) 2013. CC Attribution 3.0 License.

Atmospheric Measurement Techniques Discussions
Open Access

This discussion paper is/has been under review for the journal Atmospheric Measurement Techniques (AMT). Please refer to the corresponding final paper in AMT if available.

Characterization of In Band Stray Light in SBUV/2 Instruments

L.-K. Huang[1], M. T. DeLand[1], S. L. Taylor[1], and L. E. Flynn[2]

[1]Science Systems and Applications, Inc. (SSAI), 10210 Greenbelt Road, Suite 600, Lanham, Maryland 20706, USA
[2]NOAA NESDIS, College Park, Maryland, USA

Received: 22 July 2013 – Accepted: 20 August 2013 – Published: 28 August 2013

Correspondence to: L.-K. Huang (liang-kang.huang@ssaihq.com)

Published by Copernicus Publications on behalf of the European Geosciences Union.

Abstract

Significant In-Band Stray Light (IBSL) error at solar zenith angle (SZA) values larger than 77° near sunset in 4 SBUV/2 instruments has been characterized. The IBSL error is caused by large surface reflection and scattering of the air-gapped depolarizer in front of the instrument's monochromator aperture. The source of the IBSL error is direct solar illumination of instrument components near the aperture rather than from earth shine. We have analyzed SBUV/2 albedo measurements on both dayside and night side to develop an empirical model for the IBSL error. This error has been corrected in the V8.6 SBUV/2 ozone retrieval.

1 Introduction

Stratospheric ozone shields the Earth's biosphere from solar ultraviolet radiation (DeFabo et al., 2000), while tropospheric ozone as a pollutant impacts global health and economy (Selin et al., 2009). Atmospheric ozone plays an important role in climate change (Fiore et al., 2002). The Solar Backscattered Ultraviolet (SBUV) program for monitoring atmospheric ozone profile has spanned more than three decades (Stolarski et al., 2006). The first SBUV instrument was launched on Nimbus-7 satellite into a sun synchronized polar orbit in 1978 (Heath et al., 1975). It has been followed by 7 SBUV/2 instruments on NOAA satellites from 1985 to the present day (NOAA-9, NOAA-11, NOAA-14, NOAA-16, NOAA-17, NOAA-18 and NOAA-19) (Frederick et al., 1986). The last 4 SBUV/2 instruments are still active. SBUV/2 instruments measure backscattered terrestrial radiance in the nadir direction at 12 UV wavelengths from 252 to 340 nm with a spectral bandpass of 1.13 nm FWHM (full width at half maximum) for ozone monitoring. The incident solar irradiance at the top of atmosphere is also measured by SBUV/2 instruments on a regular basis for calibration. Measured ratios of the earth radiance to the solar irradiance (albedo) are used to derive ozone profiles (Bhartia et al., 1996, 2002). The long term SBUV ozone record provides important information to scientific

AMTD

6, 7911–7943, 2013

Characterization of In Band Stray Light in SBUV/2 Instruments

L.-K. Huang et al.

CC BY

research in climatology and meteorology, and to environmental protection efforts (Stolarski et al., 2006; Terao et al., 2007).

In the SBUV/2 spectral range, the earth radiance intensity varies by more than 3 orders of magnitude. Figure 1 shows typical spectra of radiance and albedo measured by an SBUV/2 instrument in its continuous spectral scan mode, which were taken and averaged in latitude band from 15° S to 15° N. The square signs indicate the 12 discrete SBUV/2 wavelengths for the regular ozone monitoring operation. Light at the short wavelength channels (252–298 nm), mostly absorbed by ozone before reaching ground, provides ozone density information in stratosphere (Bhartia et al., 2012). The measurements at longer wavelengths, which can reach the surface, provide limited information about the ozone distribution at low altitude. Detecting a 2 % change of ozone profile in the stratosphere requires SBUV/2 albedo measurements at the short wavelengths to be accurate to better than 1 %. With such a large dynamical signal range and stringent accuracy requirement, stray light often becomes a difficult issue in optical design and characterization of a spectrometer. There are 2 types of stray light, Out of Band Stray Light (OBSL) and In Band Stray Light (IBSL). OBSL represents contamination of the signal at the measured wavelength from light at other wavelengths due to imperfect spectral filtering. We will not discuss characterization of OBSL in this paper. IBSL is considered to represent imperfect spatial filtering of external illumination that passes through the spectral bandpass of a given wavelength channel. Analysis of stray light in the remote sensing instruments is often important part of sensor characterization. It can also serve as lessons in designs of future instruments.

SBUV/2 instruments have an 11° (FWHM) field of view, which projects approximately a square on the ground in the nadir direction. The response over this field of view was characterized in the SBUV/2 prelaunch calibrations. The instrument's sensitivity varies less than 10 % within a 10° × 10° center area, then, decreases sharply by a factor of 10^{-4} within 2° outside the center area. Such performance makes the SBUV radiance measurements well defined in geo location. Prelaunch testing did not fully simulate solar light direct illumination of surfaces on the spacecraft near the SBUV/2 instrument's

CC BY

aperture, which happens at an incidence angle nearly perpendicular to instrument's optical axis. The solar flux is 4 orders of magnitudes more intense than the earth radiance at 252 nm, as shown by the albedo values in the bottom panel in Fig. 1. Figure 2 shows sample albedo measurements at 273 nm on the same date by NOAA-18 SBUV/2 (N18) in top panel and NOAA-16 SBUV/2 (N16) in bottom panel. Both N16 and N18 were emerging from darkness into daylight in the Southern Hemisphere and moving into darkness in the Northern Hemisphere in the same week around fall equinox 2006. The N16 signal monotonically decreases in both hemispheres as solar zenith angle (SZA) increases, and approaches zero at SZA = 95° and beyond. This is consistent with expectations for a short wavelength ($\lambda < 300$ nm) that is blocked by ozone absorption before reaching ground. The N18 Southern Hemisphere data are consistent with N16, but the N18 Northern Hemisphere data show a sharp step increase between SZA = 78–80° in comparison with N16. The increased signal is still present in night side data until the satellite passes into Earth shadow (eclipse) at SZA = 118°. This behavior suggests that the source of the anomalous signal is direct solar illumination of the SBUV/2 instrument. We found significant IBSL contamination in the earth radiance measurements at the short wavelengths with the last 4 SBUV/2 flight modules (FM#5, FM#6, FM#7 and FM#8, which respectively flew on N14, N17, N18 and N19) at SZA higher than 78° approaching terminator. The magnitude of the IBSL contamination in the radiance measurements is as high as 25 % at SZA = 88°. In order to accurately retrieve stratospheric ozone in these situations, which frequently occur in polar regions, it is necessary to correct the IBSL error in the SBUV/2 radiance measurements. This paper reports our analysis and characterization of the SBUV/2 IBSL error in orbit, using the NOAA-19 SBUV/2 instrument as an example.

2 SBUV/2 instrument

Figure 3 is a schematic diagram of the SBUV/2 optical design. SBUV/2 instruments are equipped with double Ebert monochromators, which can ideally block OBSL at extinc-

AMTD
6, 7911–7943, 2013

tion rate of 10^{-6}. The monochromator covers a wavelength range from 160 to 405 nm, with a spectral band pass of 1.13 nm FWHM. SBUV/2 instruments make discrete measurements for profile ozone monitoring at nominal wavelengths of 252.0, 273.7, 283.2, 287.7, 292.4, 297.6, 302.0, 305.9, 312.7, 317.6, 331.3 and 339.9 nm (except for Nimbus-7 SBUV, which had channel-1 at 255.7 nm). It takes 24 s to scan through these 12 wavelengths, and completes the scan cycle in 32 s. The Cloud Cover Radiometer (CCR), installed side-by-side with the monochromator, makes continuous and simultaneous measurements at 378.6 nm with a 3 nm band pass to monitor earth surface reflectivity change during the spectral scan. A depolarizer in front of the monochromator is used to eliminate the polarization effects of atmospheric Rayleigh scattering, concerning strong polarity of a grating spectrometer. A diffuser plate can be deployed to reflect the solar light into the sensor's aperture after terminator crossing to measure the solar irradiance. Since the radiance measurement and the irradiance measurement share the same monochromator and CCR, the sensor's sensitivity is canceled in the albedo ratio used for ozone retrieval. Therefore, the bidirectional reflectance distribution function (BRDF) calibration of the solar diffuser, the only different element in the optical paths between the radiance and irradiance measurements, is more important than the absolute photometric calibration for the ozone retrieval. Rigorous SBUV/2 albedo calibrations are performed in laboratory before launch, and are traceable to NIST BRDF standards. The SBUV/2 diffuser reflectivity changes, from laboratory to spacecraft and from launch to many years in orbit, are monitored using an on-board mercury spectral lamp. Details of SBUV/2 calibrations can be found elsewhere in literatures (Frederick et al., 1986; Hilsenrath et al., 1995; Janz et al.,1995; DeLand et al., 2012).

Figure 4 shows a picture of an SBUV/2 instrument in the laboratory, with baffle plates installed surrounding the aperture and diffuser deployment mechanism. These plates are designed to shield the aperture from both direct solar incident radiation and spacecraft surface reflections of both solar light and earth shine. Most parts facing the aperture are anodized in black, which typically has a low reflectivity of several percent in the UV wavelength range of interest (Lowery et al., 1977). The noticeably brighter hor-

AMTD
6, 7911–7943, 2013

CC BY

izontal line in the picture is the cylindrical axle of the diffuser deployment mechanism, which reflects roof light into the camera. When the axle is illuminated with a flood light at different angles, the camera can capture the light on a different part of the axle due to the cylindrical geometry. The axle is couple centimeters above the front baffle in the picture. In orbit, the aperture is oriented downward towards the earth, and the axle is below the front baffle. When the satellite moves from the daylight to the night side near terminator, the diffuser deployment mechanism faces the sun. At SZA = 75°, solar light can graze over the edges of the baffle plates, and illuminate a portion of the axle toward the depolarizer. The entrant slit of the monochromator, 1.3 mm × 30 mm in size, is behind the depolarizer. Light scattering and reflection from optical surfaces of the depolarizer can redirect some of the light into the entrance slit within the field of view. This geometry is consistent with the finding of IBSL error onset and rapid rising around SZA = 77° shown in Fig. 2. SBUV/2 instruments use a depolarizer which consists of 4 quartz wedges. In the original instrument design, the surfaces of the 4 quartz wedges are optically contacted with each other. During thermal vacuum testing of the FM#4 instrument in 1987, two of the quartz crystal surfaces separated, causing a sharp change in the instrument's sensitivity, which was later fixed. To avoid further such problems, the last 4 SBUV/2 instruments (FM#5 through FM#8) were modified to have 1 mm air gaps between the surfaces of the depolarization wedges. Apparently, the air-gapped quartz wedges have surface scattering and reflection one order of magnitude larger than the optically contacted surfaces, which results in significant IBSL errors. Note that the CCR does not have the IBSL problem because its aperture is not covered by the depolarizer. The IBSL problem was first uncovered in N17 orbital data analysis as early as 2004. However, the last two SBUV/2 instruments to be launched on N18 and N19 could not be modified because of both flight schedule and budgetary constraints. In addition, there was no opportunity to perform laboratory tests to fully characterize the IBSL error before flight. Therefore, we have to use on-orbit SBUV/2 measurements to characterize the IBSL error.

AMTD
6, 7911–7943, 2013

CC BY

3 Characterization of IBSL

3.1 Dayside

We have identified IBSL with direct comparison of N16 and N18 albedo measurements at 273 nm in Fig. 2. This comparison includes differences in their field of views, scene reflectivity, terrain height and other atmospheric and geophysical properties. In the V8 SBUV ozone retrieval, an a priori ozone profile is constructed as an initial estimate of the ozone profile, which has a total column ozone equal to the total column ozone determined with measurements at 318 nm for ozone absorption and at 331 nm for scene reflectivity (Bhartia et al., 2012). The initial ozone profile is used to calculate albedo values at other short wavelengths in the same spectral scan, using the atmospheric backscattering forward model. The difference between the measurement and the computed albedo value, called the Initial Profile Albedo Residue (IPAR) in this paper, contains the difference between the actual ozone profile and the initial estimate, the ozone absorption cross section error, the calibration offset, as well as any IBSL error. Figure 5 shows the weekly average differences in IPAR at the same latitude between N19 and N17 near North Pole as a function of spacecraft centered solar elevation angle (SCSEA) of N19, where the N19 data are contaminated with IBSL error and the N17 data do not contain this error. The spacecraft centered coordinates, SCSEA and spacecraft centered solar azimuth angle (SCSAA), are preferred in the IBSL analysis over the reference frame on the terrain surface since IBSL is attributed to the direct solar incidence on the spacecraft rather than the earth shine. Note that in normal attitude conditions SCSEA is equal to SZA -90°. The IBSL error rises rapidly in the region between SCSEA = -15° and SCSEA = -10° (corresponding to SZA = 75–80°), and flattens between SCSEA = -10° and SCSEA = -2°. The error bars are the statistical error for the mean. Note also the offset of 3×10^{-6} at 273 nm at SCSEA = -15°, which is about 3 % of measured albedo value. This albedo offset can be a combination of calibration offsets in both N19 and N17 which have 1 % uncertainty (DeLand et al., 2012), as well as possible diurnal changes in ozone profiles due to the different local times of the measurements (Haefele et al., 2008). The offset fluctuated from week to week at different wavelengths from -2×10^{-6} to 7×10^{-6}. This is larger than the likely calibration offset or instrument noise effect, and thus is likely due to atmospheric and geophysical difference.

We estimate the IBSL error at SCSEA $=-10^{\circ}$ by subtracting the IPAR difference at SCSEA $=-15^{\circ}$ from the difference at SCSEA $=-10^{\circ}$. We also tried to use extrapolation of a straight line fitted between SCSEA $=-20^{\circ}$ and SCSEA $=-15^{\circ}$ for the offset subtraction, but found that the weekly average results were too noisy to be acceptable. We do not use this IPAR difference to determine the IBSL error at SCSEA $>-10^{\circ}$ beyond the initial step-up point because of the large uncertainty in the offset subtraction. We limit the use of the day side data to channels 2–4 (273.5, 283.1, 287.6 nm). Channel-1 is not included in this analysis because measurement noise is much more significant for the low signals at 252 nm. Determination of IBSL error at the longer wavelengths (channels 5 and up) is more difficult because the measurements are impacted more by surface reflectivity variations and other differences in atmospheric properties in the lower atmosphere. The IPAR comparison can also be limited seasonally because of variations in orbital geometry. The observed N19 IBSL error values at SCSEA $=-10^{\circ}$ are plotted as a function of time in Fig. 6.

Figure 7 shows 2 yr of data points in IPAR zonal mean comparison at 273 nm between N19 and N17. The thin solid curve is derived from a piece-wise linear fit (ΔSCSEA $=1^{\circ}$) weighted with the reciprocal of the square of the standard error. Note that this curve is not necessarily centered with respect to the spread of data points because of the weighting. A straight line is then fit to the IPAR difference between SCSEA $=-20^{\circ}$ and SCSEA $=-15^{\circ}$, and extrapolated to correct the offset. The corrected fit result is plotted as a thick solid curve. Two results come from this exercise. First, the IBSL error between SCSEA $=-10^{\circ}$ and SCSEA $=-2^{\circ}$ can be approximated well with a straight line. We will extend this linear approximation to SCSEA $=6^{\circ}$ for further analysis. Second, the smooth curve between SCSEA $=-15^{\circ}$ and SCSEA $=-10^{\circ}$ provides the shape of the rising edge of the IBSL error.

AMTD
6, 7911–7943, 2013

cc BY

3.2 Night side

To model the behavior of the dayside IBSL error for all conditions, we have to look further into the night side, where both the SCSAA and SCSEA dependence of the IBSL error can be accurately measured and characterized. Figure 8 shows typical night side IBSL data measured by N19 in just one day. The night side measurements are calibrated in the same way as daylight measurements (DeLand et al., 2012). At short wavelengths from 252 to 298 nm, earth shine signal drop rapidly to negligible level at SCSAE 6° (SZA 96°) as measured near South Pole where N19 does not have IBSL problem. At wavelengths longer than 301 nm, earth shine decreases slowly to a negligible level at SCSAE 9° (SZA 99°). The magnitude of the night side IBSL error from 252 to 340 nm increases by a factor of 2 in terms of albedo, compared to the larger spectral dependence of the day side albedo. This weaker wavelength dependence is another fact indicating that the IBSL error is caused by some metal surface reflection of direct solar incidence rather than earth shine. IBSL contamination in the albedo measurements at wavelengths longer than 306 nm is negligible small (< 0.1 %) because 2 orders of magnitudes increase in Earth albedo (Fig. 1). There is negligible IBSL error in the solar irradiance measurements since minimum solar irradiance signal is at least 4 orders of magnitudes higher than the IBSL error.

The IBSL error is not necessary a linear function of SCSEA. As shown in Fig. 8, IBSL can be fitted well (within 3 % of IBSL) between SCSEA 6° and 22° with a straight line. However, it can deviate significantly from extrapolations of the fitted line at SCSEA 27° particularly when SCSAA is high (70° in the example). To reduce uncertainty, we choose IBSL measurements at SCSEA = 6°, as close as possible to the dayside, for interpolation of the IBSL error at short wavelengths. We will first study the IBSL error at SCSEA = 18° to understand its time dependence, goniometric dependence and wavelength dependence.

CC BY

3.2.1 Separation of time dependence and goniometric dependence

Since the reflectivity of surfaces near instrument entrant slit may change with time, and the illumination of the SBUV/2 instrument will vary with season, the overall IBSL error is expected to be a product of a time dependence function and a goniometric function. A linear fit of daily IBSL measurements between SCSEA = 14° and SCSEA = 22° gives values for both the IBSL error and the rate of change dIBSL/dSCSEA at SCSEA = 18°. Figure 9a shows the derived daily IBSL error at SCSEA = 18° at 273 nm as a function of time (dots) for N19. The seasonal variations have a strong correlation with variations in SCSAA (dash curve). In order to derive any time-dependent variations in IBSL error, we first calculate relative changes of IBSL with respect to those at the same SCSAA during a reference year, April 2010 to March 2011. The normalized drift rates, derived from comparisons to reference values, are plotted in Fig. 9b. There are missing days in these raw data because SCSAA is occasionally outside the range of the reference period. The average drift rate over 4 months before April 2010 and 4 months after March 2011 is calculated to determine the drift rate during the reference period, shown by the solid line. IBSL changes during the reference period are then computed using the average drift rate, and added to the relative changes to give an initial estimate of IBSL time dependence, as shown by the dots in Fig. 9c, which is normalized to the first day of Earth radiance measurements. These values are then smoothed and interpolated with a piece-wise linear fit to get an initial estimate of the time dependence $F(t)$, shown as the solid curve.

For determination of the goniometric dependence, the IBSL daily values shown in Fig. 9a can also be plotted as a function of SCSAA, as shown in Fig. 9d. Dividing these daily IBSL values by the $F(t)$ function derived in Fig. 9c gives us the IBSL SCSAA dependence, which is now a well behaved function, as shown by the dots in Fig. 9e. A 4th order polynomial function can be used to fit the data, shown by the smooth curve, which will be called G(SCSAA). The fitted G(SCSAA) function is then used to remove the SCSAA dependence from the daily IBSL values to create a new estimate of the

AMTD
6, 7911–7943, 2013

cc BY

IBSL time dependence using all measurements, as shown by the dots in Fig. 9f. This process can be iterated if necessary. The final IBSL time dependence is shown with the smooth curve in Fig. 9f. Combining the IBSL time dependence and the IBSL SCSAA dependence,

$$\mathrm{IBSL}(t) = G(\mathrm{SCSAA}(t)) \times F(t) \tag{1}$$

we can calculate the IBSL error at SCSEA = 18°, shown by the smooth curve in Fig. 9a, where SCSAA is measured at SCSEA = 18° and is approximately constant for the range of SCSEA considered in a given day.

Daily values of dIBSL/dSCSEA at 273 nm are plotted as a function of time in dots in Fig. 10a. Apparently, dIBSL/dSCSEA is also correlated with SCSAA. Taken out the time dependence that was derived in the last paragraph, (dIBSL/dSCSEA)/$F(t)$, the normalized slope is shown as a function of SCSAA, dots in Fig. 10b. Then, the normalized slope can be fitted with a polynomial function, S (SCSAA), shown by smooth curve in Fig. 10b. We can reproduce the slope with the fitted functions,

$$\mathrm{dIBSL}/\mathrm{dSCSEA}(t) = S(\mathrm{SCSAA}(t)) \times F(t) \tag{2}$$

which is shown by the smooth curve in Fig. 10a.

3.2.2 Goniometric Functions at SCSEA = 18°

All 12 wavelength channels of daily IBSL values at SCSEA = 18° are processed to derive their goniometric functions in the same way as described in the previous section. Figure 11a shows all 12 fitted G (SCSAA, λ) functions at SCSEA = 18° for N19 as an example. Since the time dependence functions, $F(t,\lambda)$, are normalized on the first day of N19 earth view radiance measurements, G(61.1°, λ) gives IBSL at SCSEA = 18° on that day when SCSAA at SCSEA = 18° was 61.1°. The fitted polynomials are very similar to each other in shape. They can be approximated by

$$g(\mathrm{SCSAA},\lambda) = g_0(\mathrm{SCSAA}) \times C(\lambda) \tag{3}$$

Discussion Paper | Discussion Paper | Discussion Paper | Discussion Paper

AMTD

6, 7911–7943, 2013

Characterization of In Band Stray Light in SBUV/2 Instruments

L.-K. Huang et al.

Title Page | Abstract | Introduction | Conclusions | References | Tables | Figures | Back | Close | Full Screen / Esc | Printer-friendly Version | Interactive Discussion

CC BY

where g_0 (SCSAA) is an average of G (SCSAA, λ) over all wavelengths, shown as the thick solid curve, and SCSAA is taken at SCSEA = 18°. The scale factors C (λ), shown in Fig. 11b, then result in minimum standard deviations between the scaled observations and the average. The differences between the observed goniometric dependence G (SCSAA, λ) and the calculated goniometric dependence g (SCSAA, λ) are less than 0.7 % of the IBSL error, except channel-1 with a maximum of 1.2 % due to low signal level at 252 nm. Therefore, g_0 (SCSAA) is a valid approximation of the IBSL error goniometric dependence at SCSEA = 18°.

Figure 12 shows the fitted S (SCSAA) functions for the slope dIBSL/dSCSEA, normalized by the time dependence $F(t)$ at all 12 wavelengths. We can see that S (SCSAA) is essentially wavelength-independent. An average of S (SCSAA) is computed (thick solid curve). A maximum difference of 10^{-7} at SCSAA = 73° is found between the average and channel-12, which is less than 0.5 % of the IBSL error. Therefore, an average of the fitted S (SCSAA) functions can be used for the goniometric dependence of the slope.

From the above excises we conclude that the goniometric functions for IBSL and dIBSL/dSCSEA can be approximated as the combination of a wavelength-independent angular function and a wavelength-dependent scale factor. This is because the light baffle shape determines how the baffle blocks the solar light in varies solar incidence angles, which is purely geometrical. The reflection of illuminated surfaces can also have both the wavelength dependence and the angular dependence. The separation of the wavelength dependence and the angular dependence, as described above, provides a convenient and suitable approximation for the practical purpose of IBSL correction.

3.2.3 IBSL at SCSEA = 6°

The radiance measurements before the Sun rise in the south, N19 SBUV/2 near South Pole as an example in Fig. 8, show how ozone absorption blocks the solar light at UV. At SZA 99°, the albedo values at 340 nm in South is about 1 % of IBSL found in North, where the earth shine is from light scattering of atmosphere above 90 km. It dropped below sensor's noise level at SZA 100° in South, which is corresponding to a height of 100 km (N19 picks up some negligible IBSL in South starting at SCSEA 18°). Ozone absorption cross sections at wavelengths shorter than 300 nm are 2–3 orders of magnitudes larger than that at 340 nm. Therefore, solar light at the short wavelengths are completely blocked by ozone, rather than by earth eclipse, at much lower altitude before reaching SZA 96°. To estimate IBSL around SCSEA 6°, an empirical correction of the earth shine after the sunset is attempted, which scales the earth shine measurements before the sunrise with CCR values at SZA 96°,

$$I_{\text{sunset}}(\lambda, \text{SZA}) = I_{\text{sunrise}}(\lambda, \text{SZA}) \times \left[I_{\text{sunset}}(\lambda = 378\,\text{nm}, \text{SZA} = 96°)/ I_{\text{sunrise}}(\lambda = 378\,\text{nm}, \text{SZA} = 96°)\right] \quad (4)$$

where I_{sunset} and I_{sunrise} are in the albedo values. This is considered as a zero order approximation. The resulted IBSL after the earth shine correction are plotted in thick solid curve in Fig. 8. This earth shine correction has no impact at the short wavelengths at SCSEA 6°. At the long wavelengths, residues of earth shine correction contribute to noise in daily IBSL values at SCSEA 6° about 1–2 % in terms of STDV (with a peak-to-peak noise of 10 % of IBSL), which is negligible in comparison with albedo values in daylight. The daily IBSL values at SCSEA 6° are derived from a smooth function fit over SCSEA 6° and 12°. The resulted daily IBSL values at 273 nm is plotted in Fig. 6.

Estimated daily IBSL values at SCSEA = 6° are then processed for the separation of time dependence and goniometric dependence terms in the same way as described in Sect. 3.2.1. Figure 13 shows the time dependence functions, $F(t, \lambda)$, at all 12 wavelengths. The results at SCSEA = 6° are consistent with that at SCSEA = 18°. For example at 273 nm, the calculated relative IBSL error at SCSEA = 6° decreased to 0.751 at the end of August 2011, compared to a calculated value of 0.775 at SCSEA = 18° shown in Fig. 9f. Note that long wavelength channels have a lower drift rate than the short wavelength channels. This is a typical behavior in metal surface reflectivity in UV in the processes of photo carbonization of prelaunch contamination on the spacecraft.

AMTD
6, 7911–7943, 2013

The calculated SCSAA dependence of the IBSL error as a function of wavelength at SCSEA = 6°, G (SCSAA, λ), is plotted in Fig. 14a. These curves share a similarity in shape, consistent with Fig. 11a. However, only the short wavelength channels 2–6 are close to each other in shape to high accuracy (0.7 %). Large differences are found with the other channels due to the limitation at SCSEA = 6°, earth shine contamination at long wavelengths and low solar flux at 252 nm. However, the percentage of IBSL errors at the long wavelengths is negligible small, and the 252 nm channel is not used in the V8.6 SBUV/2 profile retrieval. Therefore, we take average over only channels 2–6 for the wavelength independent factor, g (SCSAA), shown in thick solid curve. The scale factors, $C(\lambda)$ shown in Fig. 14b, result in least squares of deviation between g (SCSAA) × $C(\lambda)$ and G (SCSAA, λ), which are less than 0.25 % in STDV for channels 2–6. Selection of these 5 short wavelength channels for the average guarantee the accuracy for IBSL error corrections in the ozone profile retrieval. We believe this average is a better representation of the goniometric dependence for the other long wavelength channels and that at 252 nm. The wavelength dependence of $C(\lambda)$ at SCSEA = 6° is characteristically comparable to that at SCSEA = 18° shown in Fig. 11.

Estimation of the IBSL error in daylight (SZA < 88°) has to be based on interpolation of the derived values at SCSEA = −10° and SCSEA = 6°. The weekly IPAR results at SCSEA = −10° are smoothed and interpolated to daily values with the piecewise linear fitting function, as shown in Fig. 6 for N19 at 273 nm. The slope, dIBSL/dSCSEA, is then computed with straight lines connecting the two points. Next, the time-independent normalized slope at SCSEA = 6°, S (SCSAA, λ) = (dIBSL/dSCSEA)/$F(t)$, is calculated, as shown in Fig. 15 for N19 as an example. As discussed in Sect. 3.1, we can only obtain valid dayside IBSL at the 6 short wavelengths. Among them, channel-1 has low signal, and channels 5 and 6 has some scene noise. Therefore, relatively reliable results of S (SCSAA) can be obtained only with channels 2–4. The difference in S (SCSAA) among channels 2–4 equates to only 2 % of the IBSL error at the midpoint between SCSEA = −10° and SCSEA = 6°. Therefore, the wavelength dependence of S(SCSAA) between SCSEA = −10° and SCSEA = 6° is negligible at least among these

CC BY

short wavelength channels. This is consistent with the finding at SCSEA = 18° that the normalized slopes are approximately wavelength independent. Therefore, the average of S (SCSAA) over Channels 2–4 is calculated and used to represent the normalized slope at all wavelengths.

3.3 IBSL corrections

Based on above discussions and results, we can model IBSL between SCSEA = −10° and SCSEA = 6° with the following function:

$$\mathrm{IBSL}(\mathrm{SCSEA}, t, \lambda) = [g_0(\mathrm{SCSAA}(t)) \times C(\lambda) + S(\mathrm{SCSAA}(t)) \times (\mathrm{SCSEA} - 6)] \times F(t, \lambda) \quad (5)$$

where the goniometric functions, g_0, C and S, and the time dependence function, F, are derived and defined at SCSEA = 6°, and SCSAA(t) is measured at SCSEA = 6° and is approximately constant in a given day. An average of the rising edge of the IBSL error between SCSEA = −15° and SCSEA = −10° over multiple years, which is derived as described in Sect. 3.1, is scaled to be connected with the straight line of IBSL(SCSEA, t, λ) at SCSEA = −10°.

We have examined data from all SBUV/2 instruments for IBSL errors. The instruments that use a depolarizer with optically-contacted prism elements (N9, N11, N16) have IBSL errors less than 1.5×10^{-6} in terms of albedo, which is about 20 times less than the instruments that use a depolarizer with air-gapped prisms (N14, N17, N18, N19). Therefore, the IBSL contamination in N9, N11 and N16 albedo measurements is less than 1 % even at SZA = 88°, which is not significant for practical purposes. We have used the model described here to develop separate empirical IBSL correction functions for the N14, N17, N18 and N19 SBUV/2 instruments. These corrections are implemented in the ozone processing code for the current NOAA SBUV/2 operational data processing, as well as for the SBUV/2 V8.6 reprocessing product (DeLand et al., 2012; Bhartia et al., 2012). The estimated uncertainty of the IBSL correction is less than 5 % of the error between SZA = 80° and SZA = 88°, which represents about 1 %

AMTD
6, 7911–7943, 2013

CC BY

in the earth radiance measurements at 273 nm. Figure 16 shows an example of N19 albedo measurements after IBSL correction.

4 Conclusions

IBSL is found in the earth radiance measurements by last 4 flight models of SBUV/2 instruments at SZA larger than 77° when approaching terminator. The source of IBSL is from direct solar illumination of the spacecraft rather than from earth shine. Large surface reflection and scattering that are associated with the air-gapped depolarizer result in significant IBSL. We have characterized IBSL between SCSEA = −10° and SCSEA = 6° with a linear function of SCSEA, and made IBSL correction in V8.6 SBUV/2 ozone retrieval with an uncertainty of 1 % of albedo values.

References

Bhartia, P. K., McPeters, R. D., Mateer, C. L., Flynn, L. E., and Wellemeyer, C.: Algorithm for the estimation of vertical ozone profile from the backscattered ultraviolet technique, J. Geophys. Res., 101, 18793–18806, 1996.

Bhartia, P. K., McPeters, R. D., Flynn, L. E., Taylor, S., Kramrova, N. A., Frith, S., Fisher, B., and DeLand, M.: Solar Backscatter UV (SBUV) total ozone and profile algorithm, Atmos. Meas. Tech. Discuss., 5, 5913–5951, doi:10.5194/amtd-5-5913-2012, 2012.

DeFabo, E. C.: Ultraviolet-B radiation and stratospheric ozone loss: potential impacts on human health in the Arctic, Int. J. Circumpolar Health, 59, 4–8, 2000

DeLand, M. T., Taylor, S. L., Huang, L. K., and Fisher, B. L.: Calibration of the SBUV version 8.6 ozone data product, Atmos. Meas. Tech., 5, 2951–2967, doi:10.5194/amt-5-2951-2012, 2012.

Fiore, A. M., Jacob, D. J., and Field, B. D.: Linking ozone pollution and climate change: The case for controlling methane, Geophys. Res. Lett., 29, 1919, doi:10.1029/2002GL015601, 2002.

AMTD

6, 7911–7943, 2013

Characterization of In Band Stray Light in SBUV/2 Instruments

L.-K. Huang et al.

CC BY

Frederick, J. E., Cebula, R. P., and Heath, D. F.: Instrument characterization for the detection of long-term changes in stratospheric ozone: An analysis of the SBUV/2 radiometer, J. Atmos. Ocean. Technol., 3, 472–480, 1986.

Haefele, A., Hocke, K., Kämpfer, N., Keckhut, P., Marchand, M., Bekki, S., Morel, B., Egorova, T., and Rozanov, E.: Diurnal changes in middle atmospheric H_2O and O_3: Observations in the Alpine region and climate models, J. Geophys. Res., 113, D17303, doi:10.1029/2008JD009892, 2008.

Heath, D. F., Krueger, A. J., Roeder, H. A., and Henderson, B. D.: The Solar Backscatter Ultraviolet and Total Ozone Mapping Spectrometer (SBUV/TOMS) for Nimbus G, Opt. Eng., 14, 323–331, 1975.

Heath, D. F., Wei, Z., Fowler, W. K., and Nelson, V. W.: Comparison of spectral radiance calibrations of SBUV-2 satellite ozone monitoring instruments using integration sphere and flat-plate diffuser techniques, Metrologia, 30, 259–264, 1993.

Hilsenrath, E., Cebula, R. P., DeLand, M. T., Laamann, K., Taylor, S., Wellemeyer, C., and Bhartia, P. K.: Calibration of the NOAA 11 SBUV/2 ozone data set from 1989 to 1993 using in-flight calibration data and SSBUV, J. Geophys. Res., 100, 1351–1366, 1995.

Janz, S., Hilsenrath, E., Butler, J., Heath, D. F., and Cebula, R. P.: Uncertainties in radiance calibrations of backscatter ultraviolet (BUV) instruments, Metrologia, 32, 637–641, 1995.

Lowery, J. R.: Solar absorption characteristics of several coatings and surface finishes, NASA Technical Memorandum, TM X-3509, 1977.

Selin, N. E., Wu, S., Nam, K. M., Paltsev, S., Prinn, R. G., and Webster, M. D.: Global health and economic impacts of future ozone pollution, Environ. Res. Lett., 4, 044014, doi:10.1088/1748-9326/4/4/044014, 2009.

Stolarski, R. S. and Frith, S. M.: Search for evidence of trend slow-down in the long-term TOMS/SBUV total ozone data record: the importance of instrument drift uncertainty, Atmos. Chem. Phys., 6, 4057–4065, doi:10.5194/acp-6-4057-2006, 2006.

Terao, Y. and Logan, J. A.: Consistency of time series and trends of stratospheric ozone as seen by ozonesonde, SAGE II, HALOE, and SBUV(/2), J. Geophys. Res., 112, D06310, doi:10.1029/2006JD007667, 2007.

AMTD
6, 7911–7943, 2013

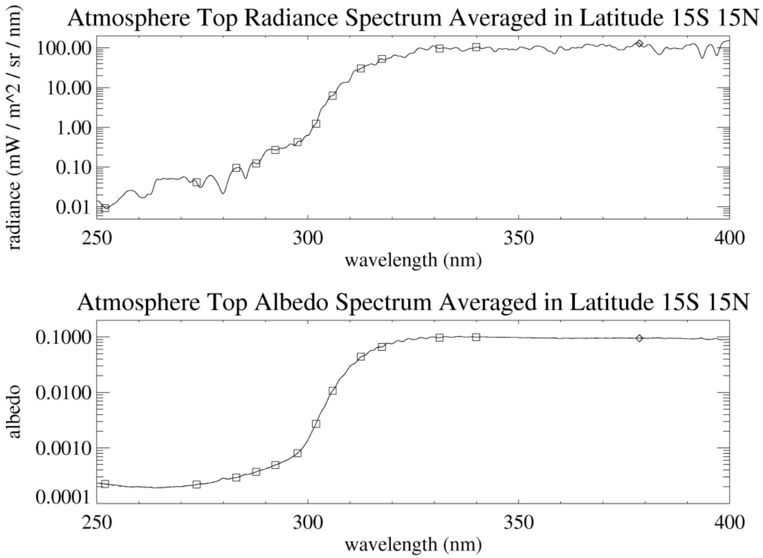

Fig. 1. Solar backscattered ultraviolet spectrum measured by NOAA-16 SBUV/2. The monochromator completes a spectral scan in 168 seconds. The radiance spectrum (top panel) is an average of 60 scans between latitude 15° S and 15° N. The albedo spectrum (bottom panel), equal to the radiance spectrum divided by the solar irradiance spectrum, is used in the ozone retrieval. Square symbols represent SBUV/2 discrete wavelengths used for ozone measurements. The diamond shows the location of the cloud cover radiometer (CCR) measurements.

AMTD
6, 7911–7943, 2013

CC BY

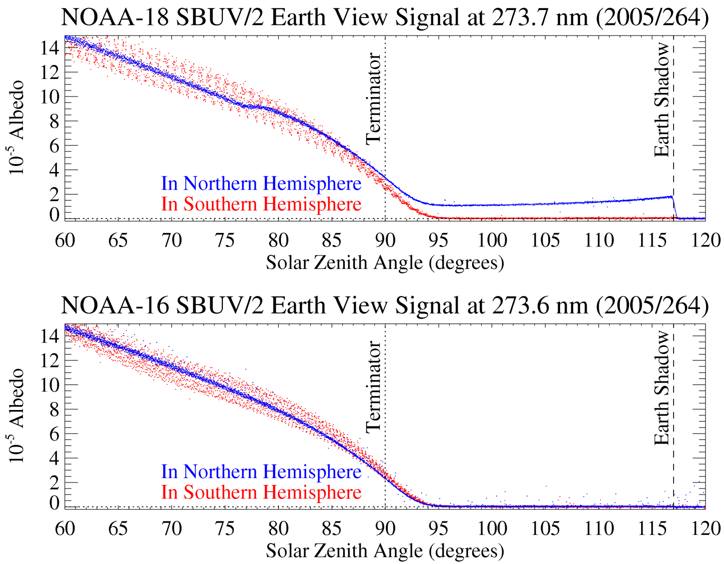

Fig. 2. Comparison of SBUV/2 earth view (radiance) signals at 273 nm between NOAA-18 (top panel) and NOAA-16 (bottom panel). The IBSL error in NOAA-16 data is negligible. NOAA-18 SBUV/2 data have significant IBSL error at SZA > 77° approaching the terminator in the Northern Hemisphere.

AMTD
6, 7911–7943, 2013

CC BY

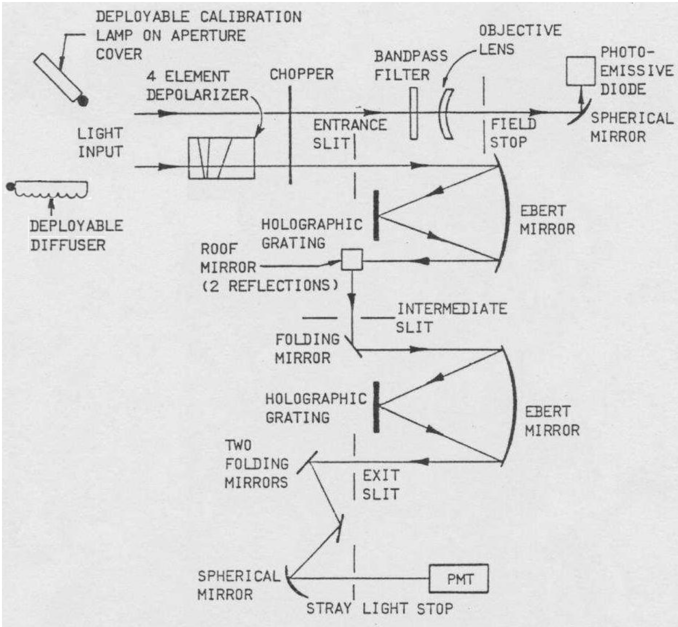

Fig. 3. Diagram of SBUV/2 instrument optics. SBUV(/2) instruments consists of double Ebert monochromators for scanning ozone absorption wavelengths, and a bandpass-filter photometer as a cloud cover monitor. A depolarizer is installed in front of the monochromator to minimize the polarization effect with atmosphere Rayleigh scattering coupled with strong polarity with the grating spectrometer. Courtesy Ball Aerospace and Technologies Corp.

AMTD
6, 7911–7943, 2013

Characterization of In Band Stray Light in SBUV/2 Instruments

L.-K. Huang et al.

CC BY

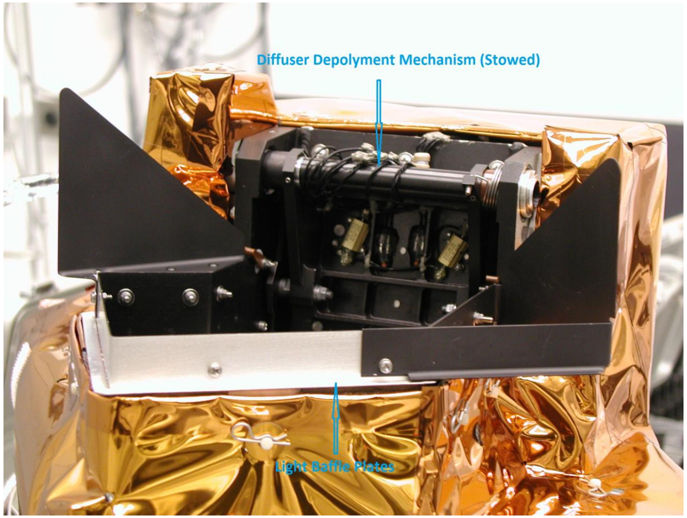

Fig. 4. SBUV/2 instrument in the laboratory. Pieces of anodized plates are installed surrounding the SBUV/2 aperture as light baffles. The diffuser deployment mechanism has a cylindrical axle that reflects roof light into the viewer's eye. Courtesy Ball Aerospace and Technologies Corp.

AMTD
6, 7911–7943, 2013

CC BY

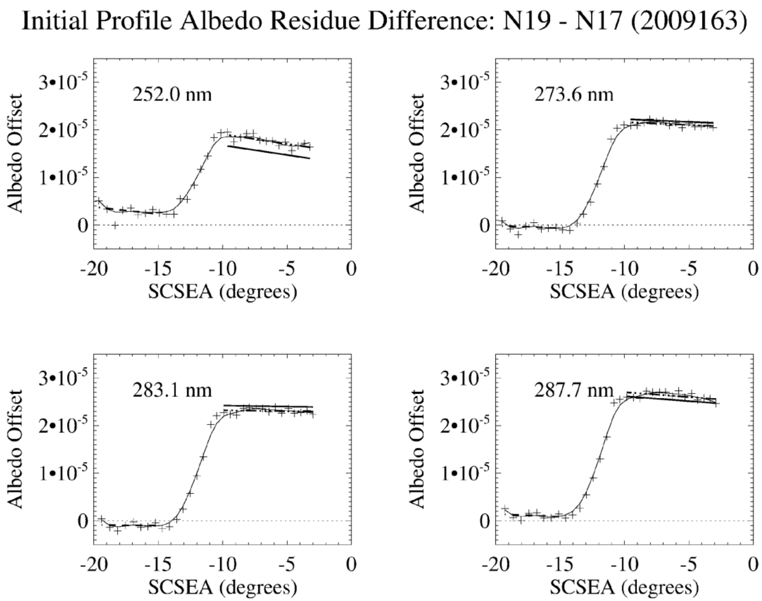

Fig. 5. Initial profile albedo residue (IPAR) comparison between NOAA-19 and NOAA-17 in northern hemisphere, where N19 is contaminated with IBSL and N17 is clean. The comparison is made at the same latitude band of 0.5 degrees in weekly average. The difference is plotted against N19 SCSEA.

AMTD
6, 7911–7943, 2013

Characterization of In Band Stray Light in SBUV/2 Instruments

L.-K. Huang et al.

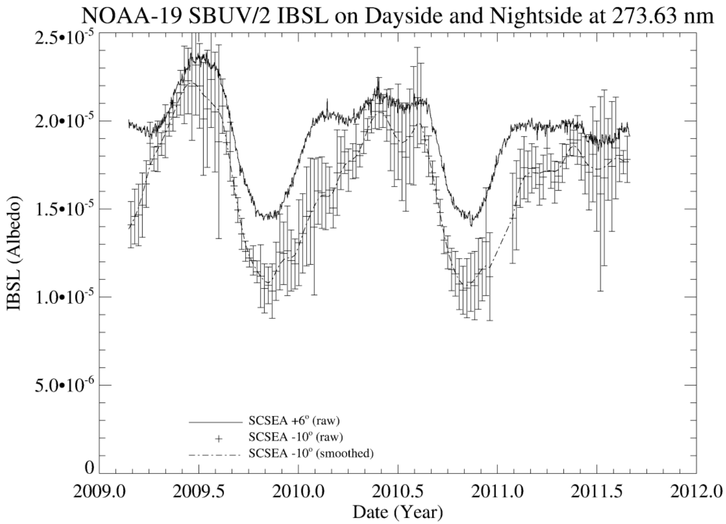

Fig. 6. N19 IBSL error values derived from measurements at 273 nm at SCSEA = –10° and SCSEA = 6°. Weekly averages at 273 nm at SCSEA = –10° (triangles) are derived from comparison of IPAR with N17. N19 IBSL error values at SCSEA = 6° are derived from daily Earth view measurements on the night side (see Sect. 3.2).

AMTD
6, 7911–7943, 2013

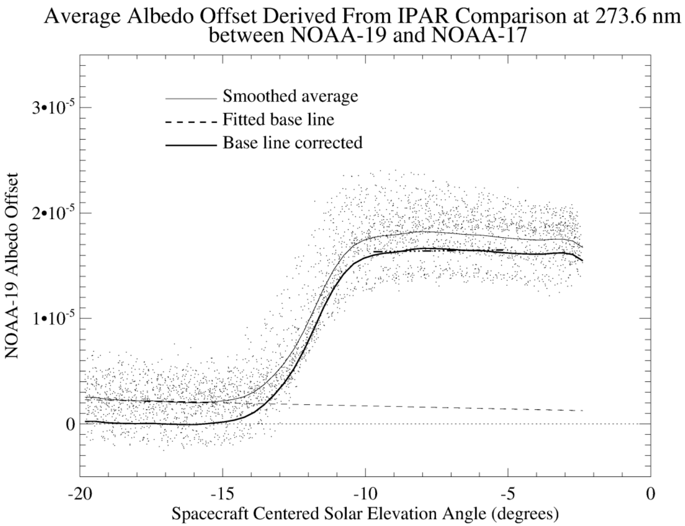

Fig. 7. Two years of data points from IPAR comparison between N19 and N17 in north illustrate the IBSL error at 273 nm as a function of SCSEA, a rapid rising edge and flat top before and after SCSEA = −10°. Piece-wised linear fitting, weighted with statistical error of each point, is used to get a smooth average (thin solid curve). Then, it is corrected for back ground offset which is an extrapolation of a straight line fitted between SCSEA = −20° and SCSEA = −15° (in dash line). The final result for IBSL is plotted in thick solid curve.

AMTD
6, 7911–7943, 2013

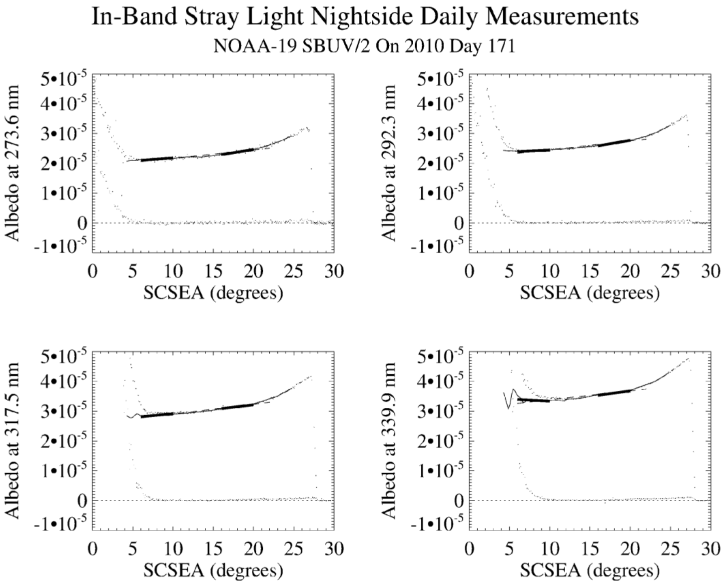

Fig. 8. Example of N19 IBSL night side daily measurements on night side on 2010 Day 171. Larger IBSL errors are measured in the Northern Hemisphere, and lower signals are in south. Thin solid curves are for IBSL after the empirical correction of earth shine near terminator, which become noisy at SCSEA = 4°. Therefore, we use data only at SCSEA > 6°. Thick straight lines are respectively fitted between SCSEA = 6°–10° for daily IBSL at SCSEA = 6°, and between SCSEA = 16°–20° for daily IBSL at SCSEA = 18°.

CC BY

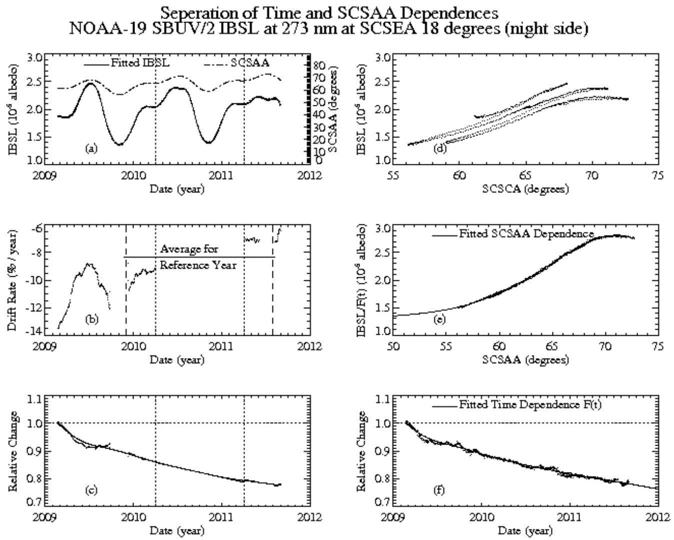

Fig. 9. N19 IBSL at 273 nm at SCSEA = 18° is a product of time dependence and SCSAA dependence. **(a)** Daily IBSL values (dots) are highly correlated with SCSAA (dash curve), and can be represented by $F(t) \times G$ (SCSAA) (solid curve). **(b)** Average drift rates are derived from comparison of daily IBSL values at the same SCSAA. Missing data are due to SCSAA values outside the range in the reference period. **(c)** Initial estimate of IBSL time dependence is derived from the comparison of daily IBSL values at the same SCSAA, and from the average drift rate for the reference period. It is smoothed and interpolated with piecewise linear fit. **(d)** Daily IBSL values before removing the time dependence are plotted against SCSAA at SCSEA = 18°. **(e)** IBSL/$F(t)$ is fitted with a polynomial of SCSAA, G (SCSAA). **(f)** Relative changes are reiterated with daily IBSL values divided by the fitted G (SCSAA), then normalized and smoothed for the time dependence function, $F(t)$.

AMTD
6, 7911–7943, 2013

Characterization of In Band Stray Light in SBUV/2 Instruments

L.-K. Huang et al.

CC BY

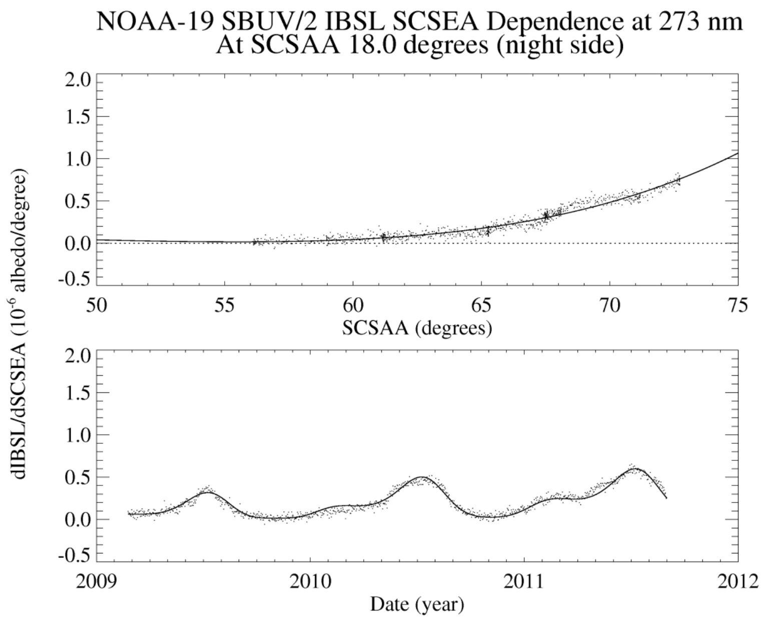

Fig. 10. (a) Daily values of the slope dIBSL/dSCSEA (dots) can be approximated with $F(t) \times S$ (SCSAA) (solid curve). **(b)** dIBSL/dSCSEA/$F(t)$ can be fitted with a polynomial of SCSAA, S (SCSAA).

AMTD
6, 7911–7943, 2013

Characterization of In Band Stray Light in SBUV/2 Instruments

L.-K. Huang et al.

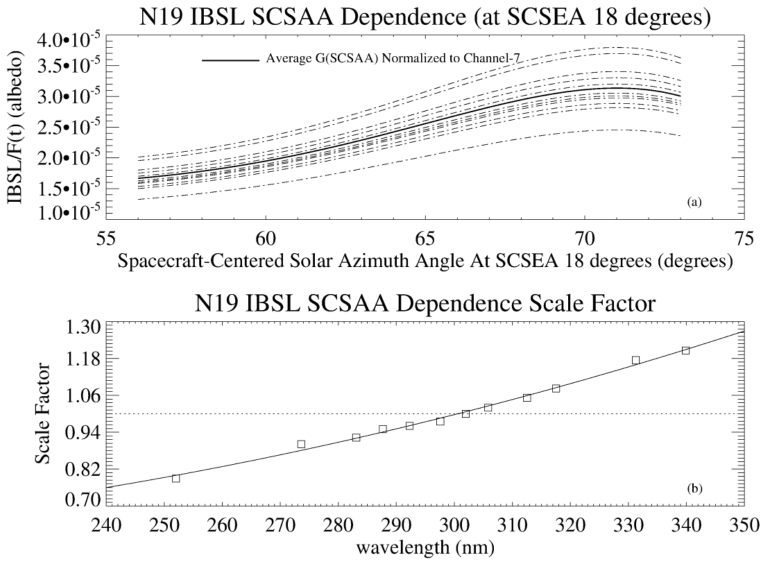

Fig. 11. Dash curves in the top panel are for 12 channels of fitted G (SCSAA) functions, which can be approximated within 0.7 % of IBSL by a product of a wavelength independent factor for the SCSAA dependence and the scale factors in the bottom panel, g_0 (SCSAA) × $C(\lambda)$.

CC BY

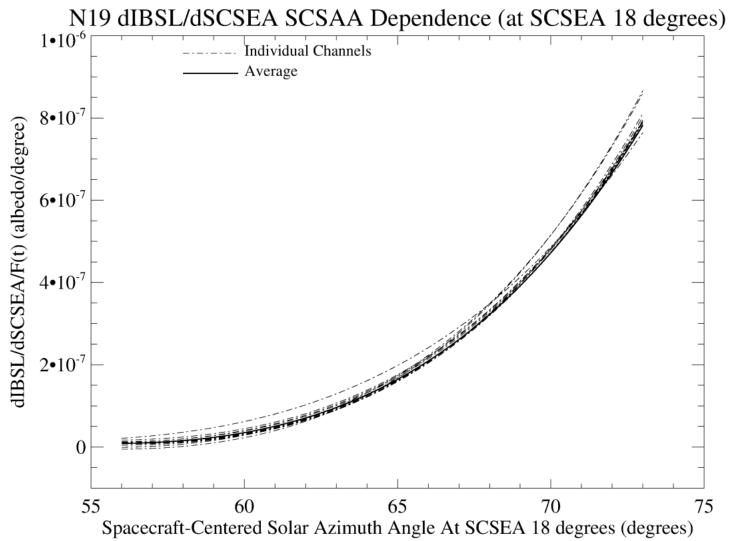

Fig. 12. Fitted S(SCSAA) functions for the IBSL slope, dIBSL/dSCSEA, at different wavelengths can be approximated with an average (solid line).

AMTD
6, 7911–7943, 2013

Characterization of In Band Stray Light in SBUV/2 Instruments

L.-K. Huang et al.

CC BY

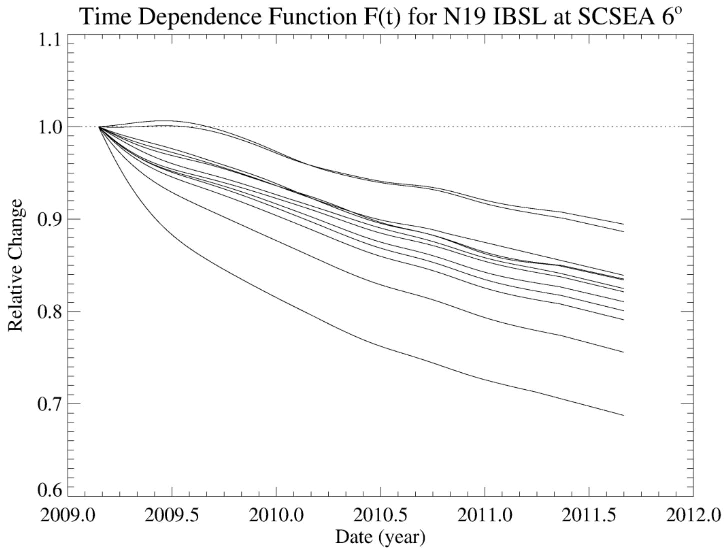

Fig. 13. Time dependence functions $F(t, \lambda)$ for N19 IBSL at SCSEA = 6°, normalized to the start of the mission. The magnitude of the overall drift monotonically increases towards shorter wavelengths. At the end of data record, the magnitude of $F(t, \lambda)$ ranges monotonically from 0.68 at 252 nm to 0.90 at 340 nm.

AMTD
6, 7911–7943, 2013

cc BY

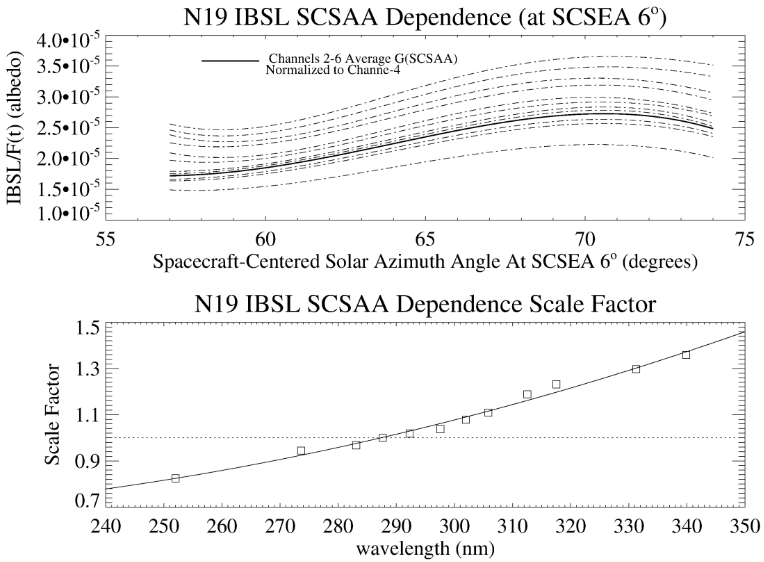

Fig. 14. Dash curves in the top panel are for 12 channels of fitted *G* (SCSAA) functions, Only channels 2–6 are averaged for the wavelength independent factor g_0 (SCSAA) because of the earth shine contamination at the long wavelengths and low signal at 252 nm. The scale factors in the bottom panel, *C* (λ), are resulted from least square between *G* (SCSAA) and g_0 (SCSAA) × *C* (λ).

AMTD
6, 7911–7943, 2013

CC BY

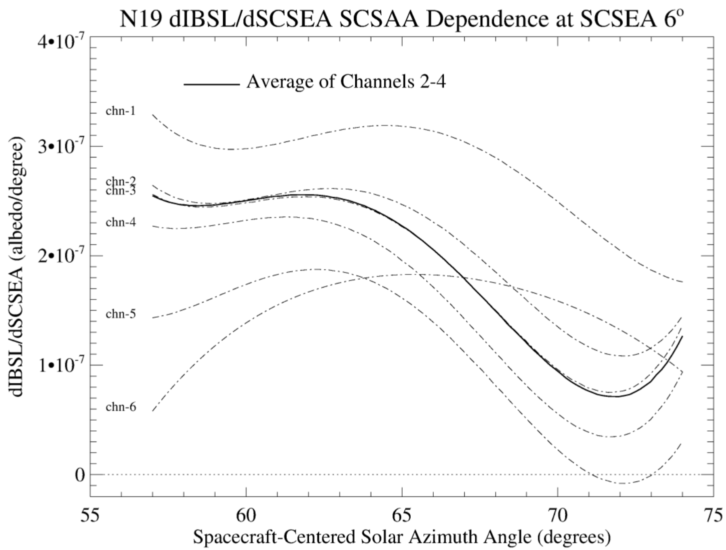

Fig. 15. N19 dIBSL/dSCSEA at SCSEA = 6° is calculated with IBSL at SCSEA = −10° in IPAR analysis on the dayside and measurements at SCSEA = 6° on the night side.

AMTD
6, 7911–7943, 2013

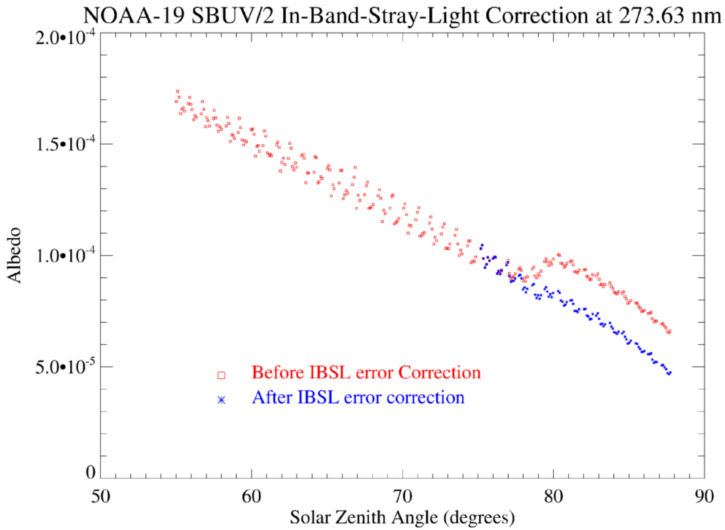

Fig. 16. Sample of N19 albedo measurements at 273 nm near North Pole before and after the IBSL correction.

AMTD
6, 7911–7943, 2013

Characterization of In Band Stray Light in SBUV/2 Instruments

L.-K. Huang et al.

CC BY